

Obtaining the spacetime metric from cosmological observations

Teresa Hui-Ching Lu and Charles Hellaby

Department of Mathematics and Applied Mathematics, University of Cape Town, Rondebosch 7701, South Africa

E-mail: Teresa.HuiChingLu@gmail.com and Charles.Hellaby@uct.ac.za

Abstract. Recent galaxy redshift surveys have brought in a large amount of accurate cosmological data out to redshift 0.3, and future surveys are expected to achieve a high degree of completeness out to a redshift exceeding 1. Consequently, a numerical programme for determining the metric of the universe from observational data will soon become practical; and thereby realise the ultimate application of Einstein's equations. Apart from detailing the cosmic geometry, this would allow us to verify and quantify homogeneity, rather than assuming it, as has been necessary up to now, and to do that on a metric level, and not merely at the mass distribution level. This paper is the beginning of a project aimed at such a numerical implementation. The primary observational data from our past light cone consists of galaxy redshifts, apparent luminosities, angular diameters and number densities, together with source evolution functions, absolute luminosities, true diameters and masses of sources. Here we start with the simplest case, that of spherical symmetry and a dust equation of state, and execute an algorithm that determines the unknown metric functions from this data. We discuss the challenges of turning the theoretical algorithm into a workable numerical procedure, particularly addressing the origin and the maximum in the area distance. Our numerical method is tested with several artificial data sets for homogeneous and inhomogeneous models, successfully reproducing the original models. This demonstrates the basic viability of such a scheme. Although current surveys don't have sufficient completeness or accuracy, we expect this situation to change in the near future, and in the meantime there are many refinements and generalisations to be added.

PACS numbers: 98.80.-k, 98.65.-r

1. Introduction

In modern cosmology, many attempts have been made to determine the large-scale structure of the physical universe using constraints provided by cosmological observations and knowledge derived from local physical experiments. The most common approach is to adopt the postulate that the universe is spatially homogeneous on large scales — the Friedmann-Lemaître-Robertson-Walker (FLRW) model. Hence using observational data to determine the few free parameters characteristic of such universe models has become the primary objective, and this overall framework has been presented in great detail in the literature.

The cosmological principle (see [6] and [32]) expresses spatial homogeneity as a point of principle, whereas the copernican principle merely states that we are not

privileged observers. As pointed out in [9], the cosmological principle determines a complete universe model, but we cannot verify it fully due to the predictions it makes about parts of the universe far beyond our observations. Although the copernican principle only has implications for the observable universe, its validity can potentially be proven with observations. Despite this, it is the much stronger cosmological principle which is almost invariably assumed in practice. Certainly, a good argument for homogeneity is provided by the Ehler-Geren-Sachs (EGS) theorem [7], which required exactly isotropic CMBR observations for all observers, and the ‘almost EGS theorem’, or Stoeger-Maartens-Ellis (SME) theorem [30], which allows small anisotropies in the cosmic microwave background radiation (CMBR) and obtains an ‘almost FLRW’ geometry [21]. But our attempts to verify homogeneity should not stop there.

The general assumption that the universe has a Robertson-Walker metric on the very large scale has served cosmology well, and is implicit in many calculations. But this makes verifying homogeneity rather tricky as there is a distinct danger of a circular argument. To analyse the cosmological data consistently requires the use of a non-homogeneous metric.

Current and planned galaxy surveys are vastly increasing the amount of cosmological data available for analysis. Already in recent years there has been a dramatic improvement in the number of measured cosmological parameters and the accuracy of their values. Properties of the matter distribution have been well studied, but always with the assumption of a homogeneous background metric. As accurate cosmological data accumulates, the proper reduction and interpretation of the high redshift data will require knowledge of the cosmic geometry that is traversed by the light rays we observe. It will no longer be necessary to assume homogeneity, the data will make it possible to quantify the level of homogeneity on different scales. Hence, being able to *prove* the homogeneity of the observable region of the universe rather than assuming it in principle is a long term objective of the current project. There are of course a variety of methods for checking homogeneity, such as the Sunyaev-Zel’dovich effect, and it is important to pursue the full range of methods.

It should be emphasised that radial homogeneity is far harder to prove clearly than isotropy. Our cosmological observations are restricted to our past null cone, which is a 3-dimensional slice through our 4-dimensional spacetime, and the expected variation of observations with redshift is affected by the cosmic equation of state, the evolution of the observed sources, and the geometry of spacetime. Disentangling these effects without assuming homogeneity is not a trivial exercise [13, 22].

We wish to determine the spacetime geometry as far as possible from astronomical observations with minimal a priori assumptions. In principle a set of observations of the redshifts, angular diameters, and apparent luminosities of galaxies, as well as their number counts, combined with knowledge of the cosmic equation of state and the true diameters, luminosities and masses of the sources (and the evolution of these source properties), can be turned into metric information. The idea of reducing observed cosmological data to a metric was first explicitly discussed by Kristian and Sachs [17]; they examined how this could be done near our present spacetime position by deriving expressions in power series for some astronomical observations near the observer in a general metric, and demonstrated the difficulties faced in confirming homogeneity of the universe from observations. However, the problem of source evolution was barely addressed in their derivations. In the ideal observational cosmology program by Ellis and Stoeger and others [1–3, 11, 19, 23, 24, 26–29], they took a slightly different

approach to Kristian and Sachs as they aimed to determine what could and could not be decidable in cosmology on the basis of ideal astronomical observations, and so considered the limits of verification in cosmology. They worked with observational coordinates since all observational data are given, not on the usual spacelike surface of constant time, but rather on our past null cone, which is centred at our observational position on our worldline. Hence, the observational data can be used with ease in the implementation of any algorithm developed through using the Einstein field equations (EFEs) that are written in observational coordinates.

Thus there has been a fair bit of theoretical work on how to determine the cosmic metric from standard observations, but implementation has not been attempted and the two key issues of choosing appropriate numerical methods and handling real observational data have not been properly addressed. However Bishop and Haines [4] did make a numerical attack on the problem that was only partly successful. They treated the past null cone (PNC) as a time-reversed characteristic initial value problem (CIVP). Since the CIVP code is not intended to deal with a reconverging past null cone, their numerics blew up at the maximum in the diameter distance, and they were not able to extend past this point[‡]. As shown here, careful consideration of the nature of this maximum allows the integration to be continued to much higher redshifts. This is clearly a very big task, and will take years to develop into a rigorous algorithm generating believable results. We here describe the beginnings of such a procedure, necessarily simple at first. Our focus here is on turning the theoretical algorithm outlined in [22] into a workable numerical method, and thereby providing a demonstration of the viability of a key component of the problem. In tackling a problem of this magnitude, it is essential to start simply, which is the main reason for initially assuming spherical symmetry and zero cosmological constant. In the long term we envisage a much more general treatment. (We note however, that we are unavoidably at the centre of our past null cone, and spherical coordinates provide a natural description.) Even this simple first step provides some interesting challenges, which are discussed below. Our expectation is that the accuracy and especially the completeness of cosmological redshift surveys will be much enhanced in the coming years, and extracting the geometric implications of the observations will become possible.

2. The Lemaître-Tolman-Bondi Model and its null cone relations

The general spherically symmetric metric for an irrotational dust matter source in synchronous comoving coordinates is the Lemaître-Tolman-Bondi (LTB) [5, 18, 31] metric

$$ds^2 = -dt^2 + \frac{[R'(t,r)]^2}{1+2E(r)} dr^2 + R^2(t,r)d\Omega^2, \quad (1)$$

where $R'(t,r) = \partial R(t,r)/\partial r$, and $d\Omega^2 = d\theta^2 + \sin^2\theta d\phi^2$. The function $R = R(t,r)$ is the areal radius, since the proper area of a sphere of coordinate radius r on a time

[‡] Their initial data on the PNC were the diameter distance, the 2-metric derived from image distortions, the matter 4-velocity derived from redshifts and proper motions, and the matter density derived from number counts. Knowledge of the true shapes, absolute luminosities and masses of the sources was assumed. They adapted an axially symmetric, zero pressure, zero rotation, zero Λ , CIVP code and tested it on spherically symmetric Einstein-de Sitter PNC data, finding it to be second order accurate. Although r and l are called luminosity distances throughout, it is evident from their equations and figure 4 that they are diameter distances. This work has not been followed up.

slice of constant t is $4\pi R^2$. The function $E = E(r) \geq -1/2$ is an arbitrary function of the LTB model representing the local geometry.

Solving the EFEs with $\Lambda = 0$ gives us a generalised Friedmann equation for $R(t, r)$,

$$\dot{R}^2(t, r) = \frac{2M(r)}{R(t, r)} + 2E(r) , \quad (2)$$

and an expression for the density

$$4\pi\rho(t, r) = \frac{M'(r)}{R^2(t, r)R'(t, r)} , \quad (3)$$

where $M(r)$ is another arbitrary function of the LTB model that gives the gravitational mass within comoving radius r . Here $E(r)$ also plays a dynamical role, it determines the local energy per unit mass of the dust particles. Equation (2) can be solved in terms of a parameter $\eta = \eta(t, r)$, and a third arbitrary function $t_B(r)$ which is the time of the big bang locally:

$$R = \frac{M}{2E} (\cosh \eta - 1) , \quad \sinh \eta - \eta = \frac{(2E)^{3/2}(t - t_B)}{M} ; \quad E > 0 , \quad (4)$$

$$R = M \left(\frac{\eta^2}{2} \right) , \quad \left(\frac{\eta^3}{6} \right) = \frac{(t - t_B)}{M} ; \quad E = 0 , \quad (5)$$

$$R = \frac{M}{(-2E)} (1 - \cos \eta) , \quad \eta - \sin \eta = \frac{(-2E)^{3/2}(t - t_B)}{M} ; \quad E < 0 , \quad (6)$$

for hyperbolic, parabolic and elliptic solutions respectively[§]. Specification of the three arbitrary functions — $M(r)$, $E(r)$ and $t_B(r)$ — fully determines the model. They constitute a radial coordinate choice, and two physical relationships.

2.1. The past null cone (PNC)

The notation and null cone solution used here were first developed in [20]. However, they chose to work with the parabolic LTB model, and hence, their gauge choice which locates the null cone of the observer at one instant of time is simpler. This gauge choice was generalised to all spatial sections, i.e. for all values of E , in [22]. In this latter paper, which we will call MHE, they gave a complete outline of the observer's null cone in the LTB model, and how one can relate the LTB model to observables using this more general gauge choice. Therefore, we follow the general outline given in MHE here.

On the one hand specification of the three arbitrary functions is what determines the LTB model, and on the other the angular diameter distance and the redshift space number density are what is given on the observer's past null cone. Hence, we first need to locate the null cone, and then relate the LTB arbitrary functions to the given data.

Human observations of the sky are essentially a single event on cosmological time scales, and as a result, being able to locate a single null cone is all we need here; no general solution is needed. On radial null geodesics, we have $ds^2 = 0 = d\theta^2 = d\phi^2$.

[§] However, near the origin, it is the sign of RE/M rather than E that determines the type of solution.

From (1), if the past null cone of the observation event ($t = t_0, r = 0$) (here and now) is given by $t = \hat{t}(r)$, then $\hat{t}(r)$ satisfies

$$d\hat{t} = -\frac{R'[\hat{t}(r), r]}{\sqrt{1+2E}} dr = -\frac{\widehat{R}'}{\sqrt{1+2E}} dr. \quad (7)$$

We will denote a quantity evaluated on the observer's null cone, $t = \hat{t}(r)$, by a $\widehat{\quad}$; for example $R[\hat{t}(r), r] \equiv \widehat{R}$, and we note that it is a function of r only instead of r and t . If we choose coordinate r in such a way that, on the past null cone of (t_0, r) , we have

$$\frac{\widehat{R}'}{\sqrt{1+2E}} = 1, \quad (8)$$

then the incoming radial null geodesics are given by

$$\hat{t}(r) = t_0 - r. \quad (9)$$

With our coordinate choice (8), the density (3) and the Friedmann equation (2) on the past null cone then become

$$4\pi\hat{\rho}\widehat{R}^2 = \frac{M'}{\sqrt{1+2E}}, \quad (10)$$

$$\widehat{R} = \pm\sqrt{\frac{2M}{\widehat{R}} + 2E(r)}. \quad (11)$$

The gauge equation is then found from the total derivative of R on the null cone,

$$\frac{d\widehat{R}}{dr} = \widehat{R}' + \widehat{R} \frac{d\hat{t}}{dr}, \quad (12)$$

and this, together with (8), (9) and (11)||, leads to

$$\frac{d\widehat{R}}{dr} - \sqrt{1+2E} = -\widehat{R} = -\sqrt{\frac{2M}{\widehat{R}} + 2E(r)}. \quad (13)$$

We can then obtain an expression for $\sqrt{1+2E(r)}$,

$$W(r) \equiv \sqrt{1+2E} = \left\{ \frac{1}{2} \left[\left(\frac{d\widehat{R}}{dr} \right)^2 + 1 \right] - \frac{M}{\widehat{R}} \right\} / \left(\frac{d\widehat{R}}{dr} \right), \quad (14)$$

where a new variable $W(r)$ is introduced. This expression tells us for which regions the spatial sections are hyperbolic $1+2E > 1$, parabolic $1+2E = 1$ or elliptic $1+2E < 1$, based on data obtained from the null cone. We substitute (14) into (10) and rearrange it into the form

$$\frac{dM}{dr} + \left(\frac{4\pi\hat{\rho}\widehat{R}}{\frac{d\widehat{R}}{dr}} \right) M = \left(\frac{2\pi\hat{\rho}\widehat{R}^2}{\frac{d\widehat{R}}{dr}} \right) \left[\left(\frac{d\widehat{R}}{dr} \right)^2 + 1 \right]. \quad (15)$$

The proper time from the bang surface to the past null cone along the particle worldlines is described by

$$\tau(r) \equiv \hat{t}(r) - t_B(r) = t_0 - r - t_B. \quad (16)$$

|| Although we do not strictly know the sign of \widehat{R} , it is fairly safe to assume that it is positive on our past null cone on the large scales that we are considering. From now on we take the positive sign for the right hand side of equation (11).

2.2. Redshift formula

Since the cosmological observations are given in terms of redshift rather than the unobservable coordinate r , we need to express all the relevant quantities in terms of redshift z . In order to do this, the redshift formula is developed here.

As shown in MHE and elsewhere, the redshift in LTB models is

$$\ln(1+z) = \int_0^{r_{em}} \frac{\dot{R}'(t,r)}{\sqrt{1+2E}} dr \quad (17)$$

for the central observer at $r=0$, receiving signals from an emitter at $r=r_{em}$.

We need to find the redshift z explicitly in terms of r , \hat{R} and $\hat{\rho}$, which we will later relate to observables. We differentiate (2) with respect to r , then evaluate it on the observer's past null cone, and we find

$$\frac{\hat{R}'}{\sqrt{1+2E}} = \frac{1}{\hat{R}} \left[\frac{M'}{\hat{R}\sqrt{1+2E}} - \frac{M}{\hat{R}^2} + W' \right]. \quad (18)$$

From (14), we can get the derivative of W . Using equation (10) to eliminate M' , and combining with equations (13) and (17), it now follows that

$$\frac{dz/dr}{1+z} = - \left(\frac{d^2\hat{R}}{dr^2} + 4\pi\hat{\rho}\hat{R} \right) / \frac{d\hat{R}}{dr} \quad (19)$$

with $z(r=0) = 0$. So theoretically we now have the redshift in terms of coordinate radius r from $\hat{R}(r)$ and $\hat{\rho}(r)$ directly if we integrate (19) with respect to r .

2.3. The observables and the LTB model

As explained, we are assuming a spherical metric with a central observer purely for purely pragmatic reasons — one does not tackle the full generality of a complicated problem all at once. For simplicity, we suppose there is only one type of cosmic source and we only consider bolometric luminosities as in MHE. See Hellaby [13] for a discussion of multiple source types and multicolour observations. It is assumed that the luminosity and the number density of each source can evolve with time; with the former written as an absolute bolometric luminosity L , and the latter as a mass per source, μ . Isotropy about the Earth is assumed, and we also assume that the universe is described by zero-pressure matter - ‘dust’, and galaxies or perhaps clusters of galaxies are taken as the particles of this dust.

The two source evolution functions might naturally be expressed as functions of local proper time since the big bang, $L(\tau)$ and $\mu(\tau)$. However, one cannot be sure of the age of the objects at redshift z because the bang time is uncertain in a LTB model and also because the location of the null cone is uncertain. The proper time from bang to null cone will be a function of redshift, $\tau(z)$, and the projections of the evolution functions on the null cone are written as \hat{L} and $\hat{\mu}$. Of course, $\tau(z)$ is unknown until we have solved for the LTB model that fits the data. For the sake of simplicity, we will take \hat{L} and $\hat{\mu}$ to be given as function of z , and we use l for the apparent luminosity and n for the number count observations. In practice, many observational studies of evolution express their results in terms of z .

The area distance d_D (or equivalently the diameter distance d_A) is the true linear extent of the source over the measured angular size, which is by definition the same as the areal radius of the source at the time of emission, i.e. R in the LTB model.

It multiplies the angular displacements to give proper distance tangentially and its projection onto the observer's null cone gives the quantity \hat{R} . The luminosity distance is measurable if we know the true absolute luminosity of the source at the time of emission \hat{L} . If the observed apparent luminosity is $l(z)$, then from the reciprocity theorem [8] gives the relationship between the diameter distance $d_A = \hat{R}$ and the luminosity distance d_L ¶,

$$(1+z)^2 \hat{R}(z) = d_L(z) = \sqrt{\frac{\hat{L}}{l}} d_{10} , \quad (20)$$

where $d_{10} = 10$ parsecs.

Let the observed number density of sources in redshift space be $n(z)$ per steradian per unit redshift interval, hence the number observed in a given redshift interval over the whole sky is

$$4\pi n \delta z . \quad (21)$$

Thus the total rest mass between z and $z + \delta z$ is

$$4\pi \hat{\mu} n \delta z , \quad (22)$$

where $\hat{\mu}(z) = \mu[\tau(z)]$ is the mean mass per source. Given the local proper density on the null cone $\hat{\rho}$, the total rest mass between r and $r + dr$ evaluated on the null cone is

$$\hat{\rho} \widehat{d^3V} = \hat{\rho} \frac{4\pi \hat{R}^2 \hat{R}'}{\sqrt{1+2E}} dr , \quad (23)$$

where $\widehat{d^3V}$ is the proper volume on a constant time slice. Hence, from (22),(23) and (8), we get

$$\hat{R}^2 \hat{\rho} = \hat{\mu} n \frac{dz}{dr} . \quad (24)$$

2.4. The differential equations

Most of the equations developed above are given as differential equations (DEs), and numerically DEs are easy to work with. Therefore, we need a set of DEs, that will generate the values of r , M , E and hence t_B from the observations. The LTB model implied by the observations is thus deduced.

Transforming (19) to be in terms of redshift z instead of coordinate r , we obtain the null Raychaudhuri equation

$$\frac{d\hat{R}}{dz} \frac{d^2 z}{dr^2} (1+z) + \left[\frac{d^2 \hat{R}}{dz^2} (1+z) + \frac{d\hat{R}}{dz} \right] \left(\frac{dz}{dr} \right)^2 = -4\pi \hat{\rho} \hat{R} (1+z) . \quad (25)$$

Substituting (24) into (25), using the facts that $\frac{dr}{dz} = 1/\frac{dz}{dr}$ and $\frac{d^2 r}{dz^2} = -\left(\frac{dr}{dz}\right)^3 \frac{d^2 z}{dr^2}$, rewriting it so that all terms involving \hat{R} (and hence $d\hat{R}/dz$ and $d^2 \hat{R}/dz^2$) are on one side of the equation, we then have a second order DE for $r(z)$:

$$\begin{aligned} \frac{d^2 r}{dz^2} = & \left[\frac{d\hat{R}}{dz} (1+z) \right]^{-1} \left\{ \left[\frac{d^2 \hat{R}}{dz^2} (1+z) + \frac{d\hat{R}}{dz} \right] \left(\frac{dz}{dr} \right) \right. \\ & \left. + \frac{4\pi \hat{\mu} n}{\hat{R}} (1+z) \right\} \left(\frac{dr}{dz} \right)^2 . \end{aligned} \quad (26)$$

¶ Note that equation (31) in MHE is incorrect.

Since we want to solve all our DEs (and hence get the values for our functions r , M and E) in parallel, we need to introduce a new variable such that we can rewrite (26) as two first order DEs.

We introduce a new variable $\phi = \phi(z)$, defined by

$$\frac{dr}{dz} = \phi , \quad (27)$$

and equation (26) then becomes

$$\frac{d\phi}{dz} = \left\{ \frac{1}{1+z} + \frac{\frac{d^2\hat{R}}{dz^2} + \frac{4\pi\hat{\mu}n\phi}{\hat{R}}}{\frac{d\hat{R}}{dz}} \right\} \phi . \quad (28)$$

If we transform (14) into a function of z and take square root of both sides, using the inverse of (27) we then obtain

$$W = \sqrt{1+2E} = \frac{\frac{d\hat{R}}{dz}}{2\phi} + \frac{\left(1 - \frac{2M}{\hat{R}}\right)\phi}{2\frac{d\hat{R}}{dz}} . \quad (29)$$

We substitute (24) into (15) and rewrite it as dM/dz instead of dM/dr , so together with equation (29) we then get

$$\frac{dM}{dz} = 4\pi\hat{\mu}n\sqrt{1+2E} . \quad (30)$$

Hence, equations (27)-(30) give us a set of coupled first order DEs that we use in order to generate the values for $r(z)$, $M(z)$ and $W(z)$ (or $E(z)$) from the observational data. We can then obtain the values for $\hat{\eta}$, τ and then the third arbitrary function $t_B(z)$ for the hyperbolic and elliptic cases by substituting these values into equations (4), (6) and (16), with (4) and (6) evaluated on the null cone. However, there is a borderline case – the near-parabolic case, which is needed where the exact expressions become numerically intractable. See Appendix A for the details. Note that from equation (28), if we know the values for \hat{R} and $4\pi\hat{\mu}n$, we can then solve for ϕ independently without knowing the values of r , M and W ; while solving for r , M and W depends on knowing ϕ . This property of the ϕ equation will be very useful later on.

2.5. Origin conditions

At the origin of spherical coordinates, $r = 0$, we have $R(t, 0) = 0$ and $\dot{R}(t, 0) = 0$ for all t . Hence, on the observer's past null cone equations (12) and (13) then become

$$\left. \frac{d\hat{R}}{dr} \right|_{r=0} = \widehat{R}' = \sqrt{1+2E} = 1 , \quad (31)$$

and thus $\hat{R} \approx r$ to lowest order near $r = 0$. From (10) we then find that

$$M' \approx 4\pi\hat{\rho}_0 r^2 , \quad M \approx \frac{4}{3} \pi\hat{\rho}_0 r^3 ; \quad (32)$$

and from (14) using a Taylor series for \hat{R} , and working to second order in r , we get

$$E \approx \left[\frac{1}{2} \left(\frac{d^2\hat{R}}{dr^2} \right)_0^2 - \frac{4}{3} \pi\hat{\rho}_0 \right] r^2 , \quad (33)$$

where $d^2\hat{R}/dr^2$ is finite when $r = 0$. Note that equations (32) and (33)⁺ give us $M \propto E^{3/2}$.

We can get the origin limit for $\hat{\mu}n$ from equation (24), which is

$$\hat{\mu}n \approx \frac{r^2\hat{\rho}_0}{\left.\frac{d^2\hat{R}}{dz^2}\right|_0}. \quad (34)$$

Also, if we substitute (31) into (19), after rearranging the expression, we then get the origin condition for dz/dr (and hence z)

$$\frac{dz}{dr} \approx \left.\frac{d^2\hat{R}}{dz^2}\right|_0. \quad (35)$$

The behaviour of the DEs (27)-(30) needs to be checked near the origin, i.e. $z \rightarrow 0$. Since r and z have a linear relation, we know that near the origin, $\hat{R} \sim z$, $4\pi\hat{\mu}n \sim z^2$, $d\hat{R}/dz$ is finite, $d^2\hat{R}/dz^2 = \text{finite}$ and $M \sim z^3$. Also we know that $dz/dr(0) = 1/(d\hat{R}/dz(0))$, so $\phi = \text{finite}$. Hence, our DEs are well behaved as $z \rightarrow 0$.

2.6. Apparent horizon and the maximum in \hat{R}

In the early universe, the expansion is so rapid that the light rays that are headed towards us are actually getting further away. One can consider the set of photons that are all the same time away from observation to be an incoming wavefront. As the universe slows down, there comes a moment when the area of such a wavefront is stationary, and $R(t, r)$ has reached its maximum value. The locus of such points for all incoming wavefronts is the apparent horizon. Hence, for the LTB model, the maximum of the areal radius (or diameter distance) down the null cone is where the null cone crosses the apparent horizon. We locate this point by the calculation below.

Since the apparent horizon is the hypersurface in spacetime where \hat{R} is momentarily constant, we put $d\hat{R}/dr = 0$ into (12) and using (8), (9) and (11), we get

$$\sqrt{\frac{2M}{\hat{R}} + 2E} = \sqrt{1 + 2E}, \quad (36)$$

and hence

$$\hat{R} = 2M. \quad (37)$$

We will see that this locus presents us with a particular difficulty in our numerical reduction of null cone data. Of course, in the case when the cosmological constant is not set to zero, and if we are considering both the future and the past horizon; the calculation and the analysis will be more complicated [12, 16]. See also [14] for the observational significance of this locus.

There are a few things worth considering here – our DEs become singular when we reach the maximum in the areal radius (diameter distance) \hat{R} , i.e. $d\hat{R}/dz = 0$. From equation (37) we know that at the maximum of \hat{R} , we have $\hat{R} = 2M$. If one looks at equations (29) and (30), it actually contains zero over zero at this point, and any numerical method will break down here. Further, from (19) and (28) we can see that $d^2\hat{R}/dz^2 = -4\pi\hat{\mu}n/\hat{R}$ where $d\hat{R}/dz = 0$. There is no problematic behaviour of ϕ here, as can be verified in the FLRW case. Hence, in order to carry our numerics

⁺ Note that equation (22) given in MHE is incorrect. Their expression does not allow all three cases of E .

through the maximum of \hat{R} , we need to perform a series expansion near this point for $\hat{R}(z)$, $\hat{\mu}n(z)$, $\phi(z)$, $M(z)$ and $W(z)$, as given in (B.1)-(B.5) of Appendix B.

Here, we use \hat{R}_{max} to denote the maximum in \hat{R} , and its corresponding z value is called z_m . The series are then written in powers of $\Delta z = z - z_m$. From the \hat{R} and $\hat{\mu}n$ data, we can easily determine the values of \hat{R}_{max} , $\hat{\mu}n(z_m)$ and z_m , and thus the remaining $\hat{R}(z)$ and $\hat{\mu}n(z)$ coefficients can be evaluated by simply performing a least squares fit using the data values near z_m . In order to obtain the expressions for the coefficients in the $\phi(z)$, $M(z)$ and $W(z)$ series, we need to substitute (B.1)-(B.5) from Appendix B into our DEs (27)-(29). The detailed expressions can be found in Appendix B.

From (B.12)-(B.15) we can see that all $\phi(z)$ coefficients are determinable once we know the values of z_m and all coefficients of the \hat{R} and $4\pi\hat{\mu}n$ fits. Using (27) and (B.3), the series expansion for r is simply

$$r(z) = r_0 + \phi_0 \Delta z + \frac{\phi_1}{2} \Delta z^2 + \frac{\phi_2}{3} \Delta z^3 + \frac{\phi_3}{4} \Delta z^4 + \dots, \quad (38)$$

where $r_0 = r(z_m)$ is the integration constant.

Note that M_0 is obtained directly from \hat{R}_{max} without any further information. The only problem is that expressions (B.10), (B.11) and (B.16)-(B.18) in Appendix B, all depend linearly on M_1 . Unfortunately, no information about M_1 can be obtained when we carry out the series expansion, as one can see from (B.9). Despite this, it is still possible to obtain a value for M_1 by substituting a known value (from numerical integration), say M_a at z_a , where z_a is some distance away from z_m , into (B.4) as described in more detail below.

3. Numerical procedure

3.1. Data handling and numerical method

The actual data we must use consists of redshift and apparent magnitude measurements for a large number of discrete sources, which must be sorted into redshift bins. In each bin we must calculate the total number of sources, $4\pi n \delta z$, and the average value for the diameter distance, \hat{R} .

Now the above theory treats all physical and geometric quantities, such as the density and the metric, as continuous functions of position, while the available data is a discrete set of sources. Therefore it might at first seem one should fit a smooth curve to the data in order to proceed with the integration. However, numerical methods are not continuous either, and any numerical method we might choose to solve our PNC equations with is based on discretisation of continuous DEs. Furthermore, we must be careful not to hide any inhomogeneity by smoothing on too large a scale, or introduce unintended bias by inappropriate choice of smoothing function. We note that the process of calculating averages on the redshift bins already introduces a measure of smoothing and a basic smoothing scale. We also note that higher order integration methods that use data from several different z values will also have a smoothing effect, and this is an option we are keeping open. So although statistical fluctuations in the real data may need a further degree of smoothing, we prefer to keep it to a minimum, only introducing as much as necessary. We also argue that any extra smoothing that is required should be closely tied to the numerical integration scheme, and not merely ad hoc.

An important consideration in the choice of numerical method is that the right hand sides of the DEs (27)-(30) contain not only the functions being solved for, $\phi(z)$, $r(z)$, $M(z)$ and $E(z)$, but also the given data derived from observations, $\hat{R}(z)$ and $4\pi\mu n(z)$. Since the latter are only known at discrete z values (the mid points of the z bins), methods that allow adaptive step sizes are not appropriate, and similarly evaluations of $\phi(z)$, $r(z)$, $M(z)$ and $E(z)$ significantly above or below their correct values should be avoided because there is no way to find the corresponding values of the given data. A second consideration is that with real observations, there will be statistical fluctuations and measurement uncertainties, so there is a limit to how much improvement can be gained from using higher order methods. In line with our policy of not using a more complicated method than the situation demands, we found that, with bin size (= step size) $\delta z = 0.001$, a second order Runge-Kutta method gave entirely satisfactory results when very accurate fake data was given for the data functions. These choices may change in the future once real data is used and as more factors are included.

Once $\phi(z)$, $r(z)$, $M(z)$ and $E(z)$ are determined, then $\hat{\eta}(z)$, $\tau(z)$ and $t_B(z)$ are easily obtained from the algebraic equations (9) and (4)-(6). However, at each discrete position, we are required to determine, numerically, which type of evolution we have: hyperbolic, elliptic or near-parabolic. Note that for the near-parabolic case, when E is small but not zero, we use equation (A.6) from Appendix A. As one might have noticed, equation (A.6) is in powers of $\hat{R}(2E)/M$, and this factor can be evaluated at each discrete position since we know the values for \hat{R} , E and M . Of course, the error for this approximation of the series expansion for τ has to be small, say about 10^{-7} ; if we take (A.6) up to order 3, this will give us $\left| \frac{\hat{R}(2E)}{M} \right| \approx 0.1$. Hence, if $\frac{\hat{R}(2E)}{M} > 0.1$, we use the hyperbolic case (4); if $\frac{\hat{R}(2E)}{M} < -0.1$, we use the elliptic case (6), and if $-0.1 < \frac{\hat{R}(2E)}{M} < 0.1$ we use the near-parabolic case.

A set of computer programmes* were developed that generate the values for the LTB functions M , E and t_B . Below we give a brief summary of the order of the steps followed in our programmes. To obtain the mass, energy and bang time functions (M , E and t_B respectively) from observational data and source evolution, we proceed as follows:

(i) take the discrete observed data for $l(z, \theta, \phi)$ and $n(z, \theta, \phi)$, divide it into redshift bins of chosen width δz , and in each bin average or sum it over all angles and the bin width to obtain $l(z)$ and $n(z)$. We may wish first to correct the data for known distortions and selection effects due to proper motions, absorption, shot noise, image distortions, etc.;

(ii) choose evolution functions $\hat{L}(z)$ and $\hat{\mu}(z)$ based on whatever observations and theoretical arguments may be mustered;

(iii) determine $\hat{R}(z)$ from $\hat{L}(z)$ and $l(z)$ using (20), this is then our first input data function and we have $4\pi\hat{\mu}n$ as our second input data function;

(iv) numerically integrate the DEs (27)-(30) using the redshift bins as the basic step size, and the binned data for z , \hat{R} and $4\pi\hat{\mu}n$, thus obtaining $r(z)$, $M(z)$ and $E(z)$;

(v) solve for $\hat{\eta}$, $\tau(r)$, and hence $t_B(r)$ from (4)-(6) and (16), with (4)-(6) evaluated on the null cone. Notice that $L(\tau)$ and $\mu(\tau)$ could also be found in this step.

However, at this early stage of development, steps (i)-(iii) use test data generated from a variety of model assumptions. In fact, step (iv) has four components, which

* Matlab was used for our numerical work.

are summarised below:

- Deduce the origin parameters and output for the first 3 data points, i.e. at $z = 0$, $z = (1/2)\delta z$ and $z = (3/2)\delta z$.
- Use numerical DE solvers - a second order Runge-Kutta method - for solving the DEs up to just before the maximum in \hat{R} is reached.
- Determine the point z_a where the switch to the series expansion is made, evaluate all quantities to be matched such as M_a , W_a , etc, and extend the numerics through the maximum in \hat{R} by calculating the series expansions of Appendix B for r , ϕ , M and E .
- Evaluate another matching value for switching back from the series expansion to numerical integration, and continue to solve the DEs numerically up to the limit of the data, here set to $z = 3$.

3.2. Data near the origin

Although we have already discussed how the DEs behave near the origin, from any available cosmological data that we might use, there is no data available at the origin itself, and very little in the first few redshift bins. Therefore, a method of filling in this gap is necessary in order to provide the initial values needed by the numerical integration.

If we average over all the data values within each bin, for example the \hat{R} values within a given z bin, then the average \hat{R} values that we use are located roughly in the middle of each bin. Thus we have the first value of \hat{R} at $z = \delta z/2$. We can then get the discretised versions of $d\hat{R}/dz$ and $d^2\hat{R}/dz^2$ from the first and second differences of \hat{R} . It takes two δz bins to get the first value of the first difference at $z = \delta z$ and all the values are located at $z = k\delta z$ for any positive integer k . However, it takes three δz bins to get the first value of the second difference and hence the first value of $d^2\hat{R}/dz^2$ at $z = 3\delta z/2$, therefore, all the values are located in the middle of each bin.

Since we want to have a complete set of data at each z value, we take the average of the two neighbouring first difference data points to get all our data at the half δz locations (in the middle of each bin). In doing so, we will not have data values at the origin or at $z = \delta z/2$, since the first complete data set is at $z = 3/2\delta z$. But we know that LTB is RW like near the origin due to the fact that it assumes spherical symmetry. For that reason, the series expansions of the RW expressions are used for finding the RW parameters that fit the data values at the origin and at $z = \delta z/2$, i.e. we determine the central values of H_0 (Hubble constant) and q_0 (deceleration parameter) from the data near $z = 0$. So we take the standard RW expressions for $\hat{R}(z)$ and $4\pi\hat{\mu}n(z)$ given by equations (A.1) and (A.2) in Appendix A of MHE, and we do series expansions of them near the origin, as detailed in Appendix C. The origin limits are $r(0) = 0$, $\phi(0) = d\hat{R}/dz(0) = 1/H_0$, $M(0) = 0$, $E(0) = 0$, $\hat{R}(0) = 0$ and $d^2\hat{R}/dz^2(0) = -(3 + q_0)/H_0$.

3.3. Passing through the maximum in \hat{R}

As mentioned before, a series approximation is required in the vicinity of \hat{R}_{max} , where the DEs become singular. Here all $\phi(z)$ coefficients are determinable once we know the values of z_m and all coefficients of \hat{R} and $4\pi\hat{\mu}n$. A set of ϕ values can be generated from the series expansion by substituting a set of Δz values into (B.3), for a z interval

that overlaps with our numerical results. We use the \hat{R} and $\hat{\mu}n$ values of 180 redshift bins on either side of z_m (this is a redshift interval of 0.361 which covers about 12% of the total redshift interval that we are considering here), and perform a least squares fit with these data to obtain all the coefficients for \hat{R} and $\hat{\mu}n$, and hence obtain all coefficients for ϕ . There is good agreement between the numerical and series values over a range of z values when plotted on the same graph, and there is one intersection point between the two curves before z_m (and also the closest to z_m). The intersection points here are important since they are where we match values between the series expansion and the numerical integration for ϕ . This is what we choose for z_a , and the numerically derived M at z_a becomes our M_a .

Now that we know where z_a is, we can get M_1 from z_a and M_a if we substitute them into equation (B.4), using $\Delta z = z_a - z_m$

$$M_a = M_0 + M_1(z_a - z_m) + M_2(z_a - z_m)^2 + M_3(z_a - z_m)^3 + \dots \quad (39)$$

where M_2 and M_3 are given by (B.10) and (B.11). Similarly, if we are matching the W values

$$W_a = W_0 + W_1(z_a - z_m) + W_2(z_a - z_m)^2 + \dots, \quad (40)$$

where W_1 and W_2 are given by (B.17) and (B.18). Therefore, if we match M then

$$\begin{aligned} M_1 = & \left\{ \frac{M_a - M_0}{z_a - z_m} + \frac{8\pi^2(\hat{\mu}n)_0^2}{\hat{R}_{max}} (z_a - z_m) + \frac{R_2}{2} (z_a - z_m) \right. \\ & + \left(\frac{R_2}{1 + z_m} + \frac{(\hat{\mu}n)_1 R_2}{(\hat{\mu}n)_0} + R_3 \right) \frac{(z_a - z_m)^2}{4} \\ & + \left. \frac{8\pi^2(\hat{\mu}n)_0(\hat{\mu}n)_1}{\hat{R}_{max}} (z_a - z_m)^2 \right\} / \left\{ 1 + \left(\frac{1}{1 + z_m} + \frac{(\hat{\mu}n)_1}{(\hat{\mu}n)_0} \right) \frac{z_a - z_m}{2} \right. \\ & + \left. \left(\frac{(\hat{\mu}n)_2}{3(\hat{\mu}n)_0} + \frac{(\hat{\mu}n)_1}{3(\hat{\mu}n)_0(1 + z_m)} - \frac{R_2}{3\hat{R}_{max}} \right) (z_a - z_m)^2 \right\}. \quad (41) \end{aligned}$$

Alternatively, if W is used for the matching, we have

$$\begin{aligned} M_1 = & \left\{ W_a + \frac{R_2}{4\pi(\hat{\mu}n)_0} (z_a - z_m) + \frac{4\pi(\hat{\mu}n)_0}{\hat{R}_{max}} (z_a - z_m) \right. \\ & + \frac{3R_3}{16\pi(\hat{\mu}n)_0} (z_a - z_m)^2 - \frac{(\hat{\mu}n)_1 R_2}{16\pi(\hat{\mu}n)_0^2} (z_a - z_m)^2 \\ & + \left. \frac{3R_2}{16\pi(\hat{\mu}n)_0(1 + z_m)} (z_a - z_m)^2 + \frac{2\pi(\hat{\mu}n)_1}{\hat{R}_{max}} (z_a - z_m)^2 \right\} / \\ & \left\{ \frac{1}{4\pi(\hat{\mu}n)_0} + \frac{z_a - z_m}{4\pi(\hat{\mu}n)_0(1 + z_m)} - \frac{R_2(z_a - z_m)^2}{4\pi(\hat{\mu}n)_0\hat{R}_{max}} \right\}. \quad (42) \end{aligned}$$

All our functions should connect the numerical integration ($z < z_a$) and series expansion ($z > z_a$) parts at z_a ; and from z_a , we can generate the corresponding r_a and M_a easily. With all ϕ coefficients known, a value for r_0 can be found from (38). Using (41) or (42), a value for M_1 can easily be determined.

The purpose of doing a series expansion is to extend our numerics through \hat{R}_{max} , but once this is achieved, we need to switch back to numerical integration again. It is sensible if we connect at z_J where $z_m - z_a = z_J - z_m$.

Initially, we tried matching M at the two connecting points, z_a and z_J . However, after we compared r , ϕ , M and W from our numerics with the correct curves generated

from the assumed model, the r , ϕ and M curves showed good agreement, but the W curve had jumps at the two connecting points. As anticipated, W is the least well-determined function.

We then tried to match W at both connecting points. Although this removed the two jumps in the numerical W curve, it also reduced the accuracy of the W series expansion. A key consideration is that at z_m we actually know the value of M from (B.8) if we know \hat{R}_{max} . In order to maximise the accuracy of our series expansion and minimise the jumps that appear in our W graph, we matched M at the first connecting point, and W at the second one.

This approach does not leave any visible alteration in the M curve, the jump in W at the first connecting point is still present, but better accuracy for the series expansion is obtained and the second jump is avoided. One thing worth mentioning here is that we may need to shorten the z interval for the series expansion, since with inhomogeneous data, fluctuations will be present, so if the interval is too wide compared with the fluctuations, the accuracy for our series expansion will be lower. However, this problem will only be dealt with when it has shown a significant effect on the numerics.

4. Testing the numerics

In order to test our numerical procedure, we need fake ‘‘observational data’’ for which the correct results are known. Therefore we generated sets of ‘‘observational data’’ that would be produced in a selection of LTB universes.

Although we did a full comparison of numerical output from our programme, M , E and t_B , with the correct LTB functions for a variety of different models, both homogeneous and inhomogeneous, we cannot present all our results here. Therefore, we summarise the ones we did in Table 1 below and only present a complete set of plots from one homogeneous and one inhomogeneous model in the two subsections below. In order to avoid confusion, we call the H_0 and q_0 used for generating fake data q_{0d} and H_{0d} ; and the ones our numerical procedure extracts from the data q_0 and H_0 from here on. Where the model is inhomogeneous, both pairs are the values at the origin, as explained in Section 3.2.

4.1. Homogeneous models

Amongst the homogeneous models we found that the near-parabolic models to have slightly lower accuracy. As noted above, we expect the output function with largest error to be $W = \sqrt{1 + 2E}$.

Below we present the results of the comparison for a homogeneous model with $q_{0d} = 0.49$ and $H_{0d} = 0.72$. This is the case when we have a negatively curved universe, but very close to the flat case. In Figures 1-3, the curves plotted from our numerical output using the Runge-Kutta method and the ones from the generated RW data are in very good agreement with each other, and there is only 0.02106 % difference between the curves in Figure 4. As can be seen in Figure 4, there is still a jump in W at z_a although it is barely visible, while the jump at the second matching point is no longer visible. This justifies the earlier decisions to match first M and then W at the two connections between the numerical integration parts and the series expansion part.

Table 1. Summary of all the homogeneous and inhomogeneous cases used for full comparisons between our numerics and the generated fake data.

Homogeneous cases		
Hyperbolic ($k = +1$)	Near parabolic	Elliptic ($k = -1$)
$q_{0d} = 0.45$ $H_{0d} = 0.72$	$q_{0d} = 0.49$ $H_{0d} = 0.72$	$q_{0d} = 0.8$ $H_{0d} = 0.72$
$q_{0d} = 0.1$ $H_{0d} = 0.72$	$q_{0d} = 0.51$ $H_{0d} = 0.72$	
Inhomogeneous cases		
Hyperbolic	Near parabolic	Elliptic
Varying bang time with $q_{0d} = 0.2$	Varying geometry or energy with $q_{0d} = 0.52$	Strongly inhomogeneous with $q_{0d} = 0.6$
Varying mass with $q_{0d} = 0.22$		

The τ curves in Figure 5, and the t_B in Figure 6, show good agreement between the numerical output and the correct values.

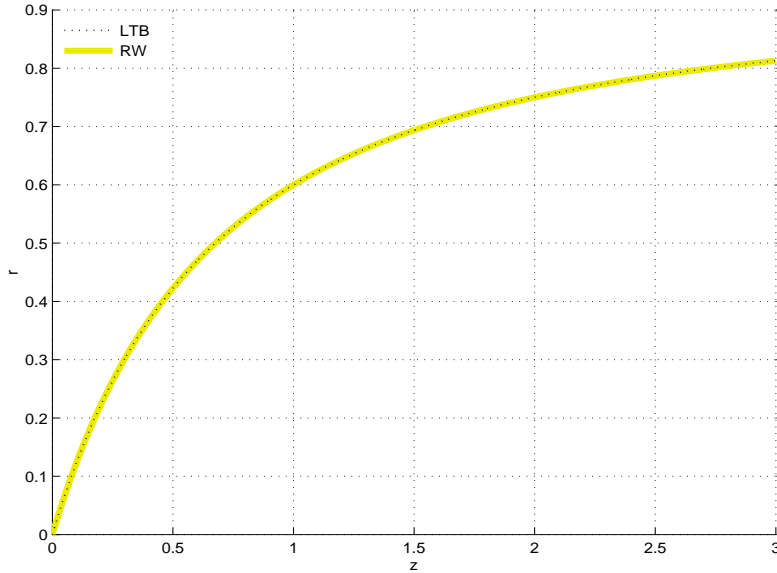


Figure 1. Results of r vs. z with $H_0 \approx 0.71999$, $q_0 \approx 0.490004$ and $\delta z = 0.001$. The grey curve is the correct RW expression and the dotted black one is our numerical output using Runge-Kutta as the integration method.

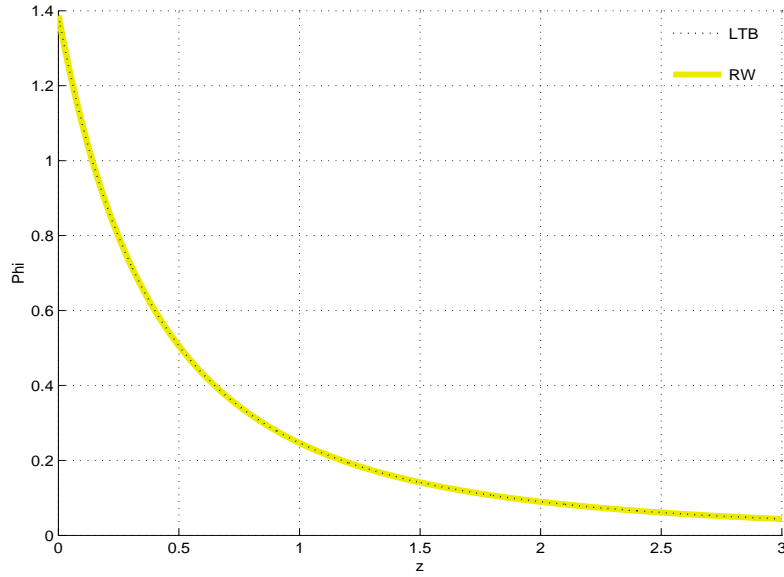


Figure 2. Results of ϕ vs. z with $H_0 \approx 0.71999$, $q_0 \approx 0.490004$ and $\delta z = 0.001$. The grey curve is the correct RW expression and the dotted black one is our numerical output using Runge-Kutta as the integration method.

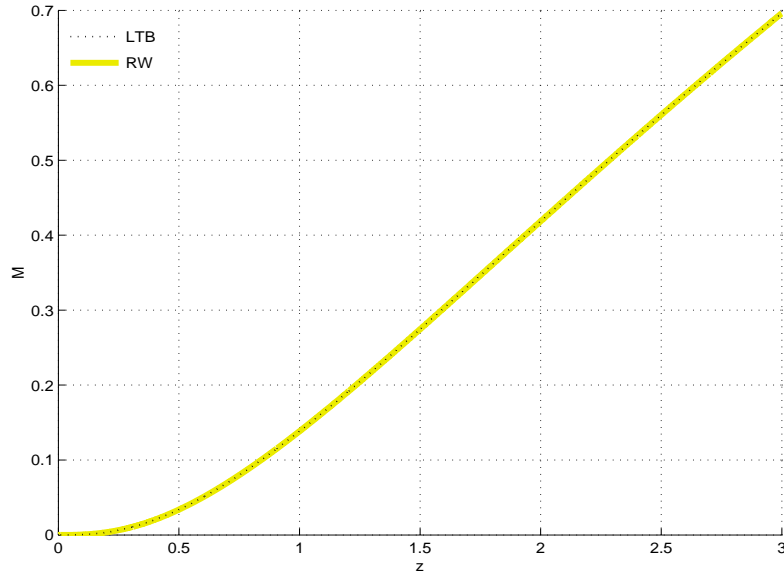


Figure 3. Results of M vs. z with $H_0 \approx 0.71999$, $q_0 \approx 0.490004$ and $\delta z = 0.001$. Matching the M values at the first connection point and the W values at the second connection point. The solid grey curve is the correct RW expression and the dotted black one is our numerical output using Runge-Kutta as the integration method.

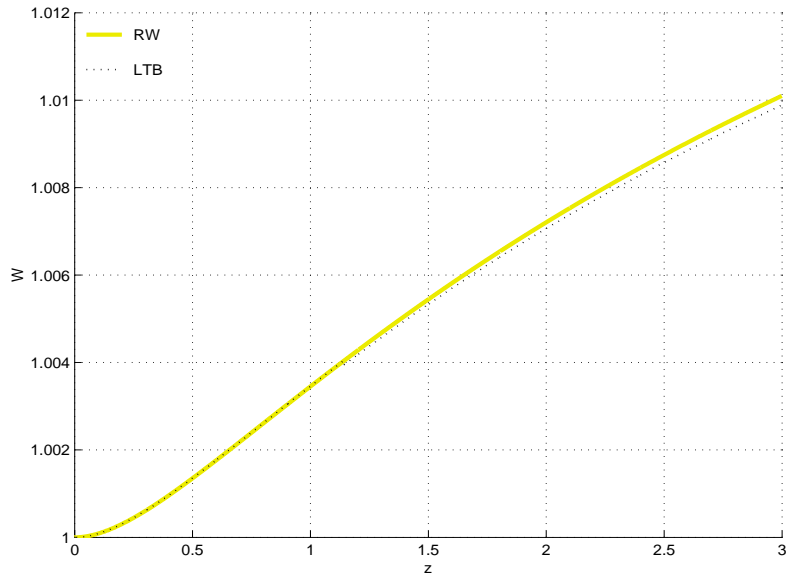


Figure 4. Results of W vs. z with $H_0 \approx 0.71999$, $q_0 \approx 0.490004$ and $\delta z = 0.001$. Matching the M values at the first connection point and the W values at the second connection point. The solid curve is the correct RW expression and the dotted one is our numerical output using Runge-Kutta as the integration method.

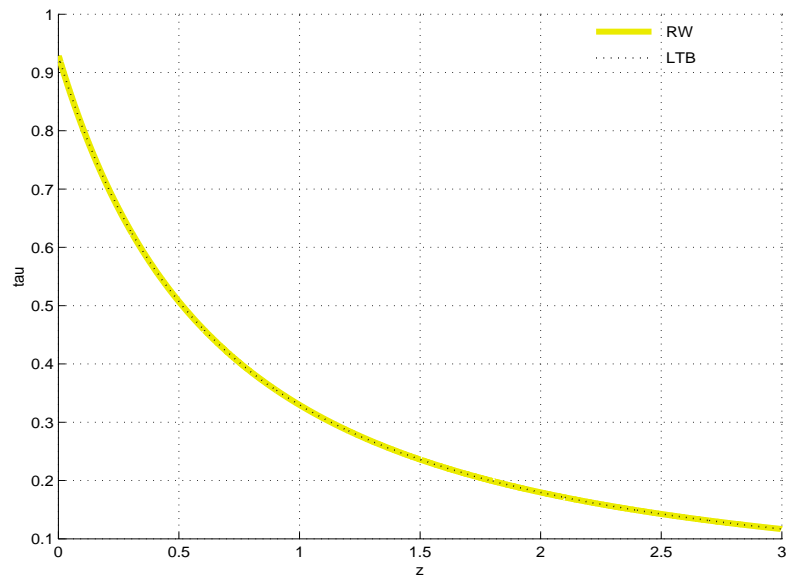


Figure 5. Results of τ vs. z with $H_0 \approx 0.71999$, $q_0 \approx 0.490004$ and $\delta z = 0.001$. The solid grey curve is the correct RW expression and the dotted black one is our numerical output using Runge-Kutta as the integration method.

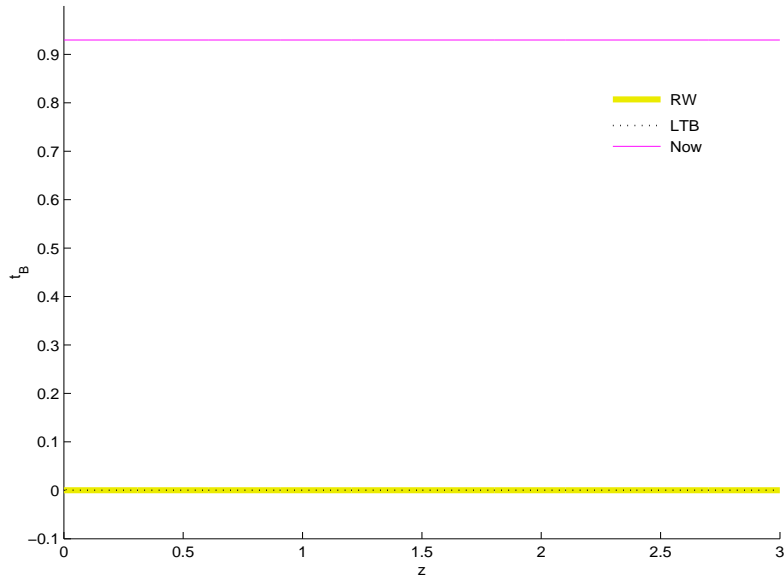


Figure 6. Results of t_B vs. z with $H_0 \approx 0.71999$, $q_0 \approx 0.490004$ and $\delta z = 0.001$. The thick solid grey curve is the correct RW expression and the dotted black one is our numerical output using Runge-Kutta as the integration method. The solid black line on the top is the current age of the universe.

4.2. Inhomogeneous models

A complete set of comparison plots from one of the inhomogeneous models tested is given here — a model with varying geometry/energy. This model is one in which the two arbitrary functions M and t_B take a RW form, while we vary the third function E .

The correct origin parameters are $H_{0d} = 0.72$, $q_{0d} = 0.52$, which gives us a near-parabolic case. The extracted values are $H_0 \approx 0.71953$ and $q_0 \approx 0.52421$. Figure 7 shows that the M curve plotted from our numerical output is slightly below the correct one; in fact there is about 2.17% error at $z = 3$. Although this percentage error is bigger than the ones we had for the homogeneous cases, this is to be expected since we are working with inhomogeneous data that was numerically generated. The percentage error is a bit larger for W , being about 26.6% as shown in Figure 8. However, this percentage error in W is large mostly because W is quite small, and we note that the absolute error in $E = (W^2 - 1)/2$ is about the same as before.

From Figures 9 and 10 we can see that the correct data and the numerical output are generally in good agreement for both τ and t_B , except near the origin. However, this is due to insufficient accuracy in the H_0 and q_0 values deduced from the “observational” data at $z = (3/2)\delta z$. Accurate values for τ and t_B depend on an accurate q_0 value, which is particularly difficult to get at the low z values near the origin. A least squares estimate of origin values, using a wider range of near-origin data may improve accuracy here.

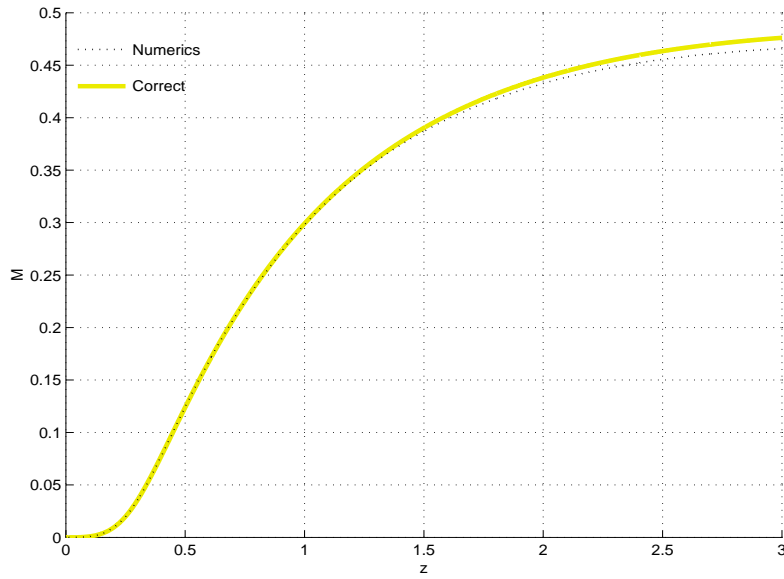


Figure 7. Results of M vs. z with $H_0 \approx 0.71953$, $q_0 \approx 0.52421$ and $\delta z = 0.001$. The solid grey curve is from the correct testing data and the dotted black curve is our numerical output using Runge-Kutta as the integration method.

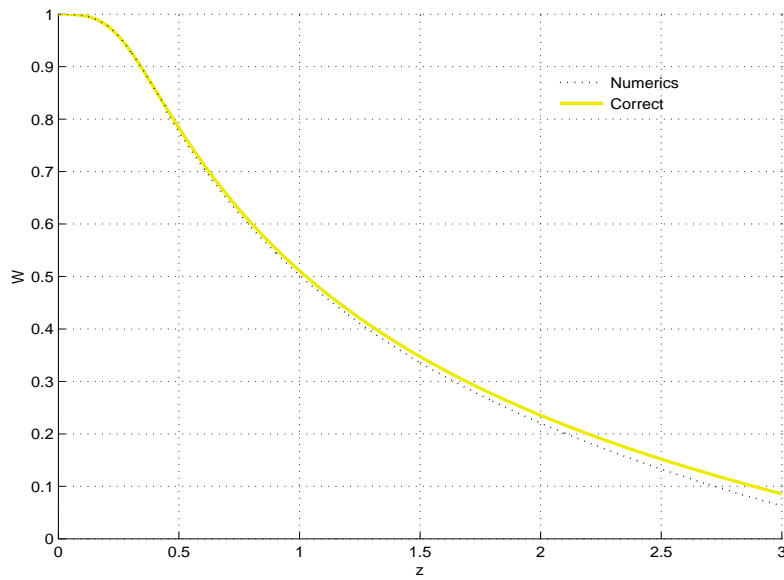


Figure 8. Results of W vs. z with $H_0 \approx 0.71953$, $q_0 \approx 0.52421$ and $\delta z = 0.001$. The solid grey curve is from the correct testing data and the dotted black curve is our numerical output using Runge-Kutta as the integration method.

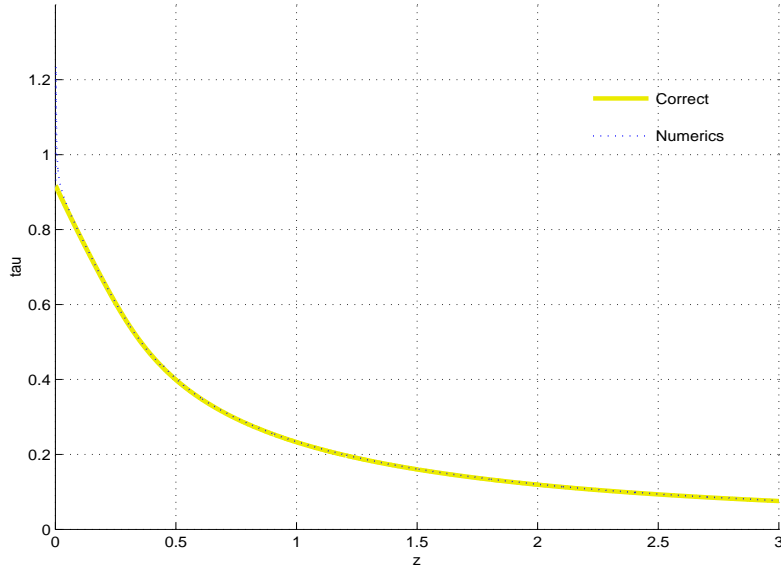


Figure 9. Results of τ vs. z with $H_0 \approx 0.71953$, $q_0 \approx 0.52421$ and $\delta z = 0.001$. The grey curve is from the correct testing data and the dotted black curve is our numerical output using Runge-Kutta as the integration method.

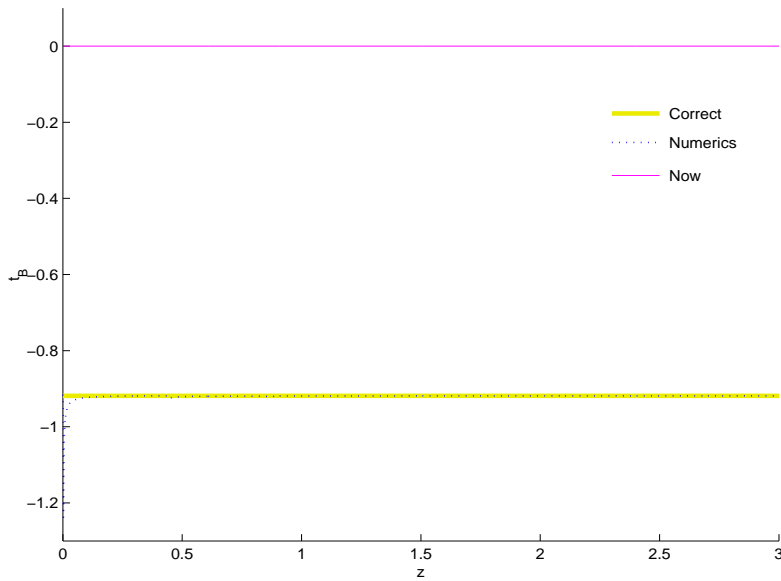


Figure 10. Results of t_B vs. z with $H_0 \approx 0.71953$, $q_0 \approx 0.52421$ and $\delta z = 0.001$. The thick solid grey curve is from the correct testing data and the dotted black one is our numerical output using Runge-Kutta as the integration method. The solid black line is the current time (origin).

5. Conclusion

We have developed a computer programme to implement the MHE algorithm. Given (spherically symmetric) data from standard observations for redshift, apparent diameter, apparent luminosity and galaxy number counts, as well as the associated evolution functions, true diameter, absolute luminosity and mass per source, it determines the metric of the (observed) universe. Its ability to reproduce the correct metric information has been tested via artificial data generated from both homogeneous and inhomogeneous models.

We have started with a very simple case, in order to understand the key elements of a numerical extraction of metric information from observations. Obviously one does not wish to tackle the full complexity of the problem at the start. Thus, there are still many improvements which can be made in both the theory and the numerical method used. Many considerations and effects must be included, for example, source evolution theories, data set completeness, different populations of sources, and more. At some point, a non-zero Λ should be considered. Also, issues like a least squares fit for the data near the origin in order to obtain better accuracy for H_0 and q_0 , and a shorter z range for the series expansion in order to carry our numerics through the point \hat{R}_{max} , also need to be dealt with for the future development. Of course, a higher order integration method may also be needed in the future in order to sustain the accuracy we have so far in our numerical output out to larger z values. However, any numerical method we use to solve the DEs must be able to handle both known data and unknown functions at a discrete set of positions. Although higher order Runge-Kutta methods will have a natural smoothing effect, some other form of smoothing of the data may be needed when we tackle real data.

The bin size used for binning the observational data will affect the accuracy of the bin averages, and require attention when one works with the real data. Using the same bin size for the whole redshift range, will leave the higher z bins flooded with data, and low z bins with very sparse data. On the other hand, making nearby redshift bins too large may impose too much smoothing. A question for the future then is the optimum binning strategy, and the choice of binning versus smoothing, given that numerical integration is ultimately a discrete process.

Our initial attempt at a numerical implementation of the MHE procedure has successfully demonstrated the viability of the basic concept, and opened the way to developing a more general treatment. Our current focus is on developing a workable numerical scheme. There are of course many relevant observational issues, such as luminosity functions, K corrections, different source populations, source evolution, bias, etc that must be incorporated in reducing the observations to the data that such a programme must use. These will be considered in the future.

Current redshift surveys do not have the accuracy or completeness to enable meaningful metric data to be extracted at present \ddagger . However, the next generation of surveys is expected to provide considerable improvements in accuracy and completeness, as well as extending to much deeper z values. Type Ia supernova

\ddagger For example, the 2dF data has large fluctuations in its number counts plot, since its thin slices were strongly affected by the individual clusters and voids encountered. Such large fluctuations would not be present in data averaged over all angles. Excessive fluctuations may cause the numerical method, which currently does not allow for angular variation, to break down, because we take first and second differences from the $\hat{R}(z)$ data. Small fluctuations in \hat{R} will generate much exaggerated fluctuations in $d\hat{R}/dz$ and $d^2\hat{R}/dz^2$.

measurements hold the promise of very good luminosity distance data in the near future, so the accuracy of luminosity functions and therefore number counts will be the limiting factor.

Current work involves analysing the stability of the DEs, ensuring the procedure can handle data with statistical scatter, estimating uncertainties in the output from uncertainties in the observational data, and using the properties of the maximum in the area distance as a means to check or correct the result.

Eventually, knowing the metric nearby will assist in analysing more distant observations in more than just a statistical sense, since the spacetime that the light rays we observe have travelled through, changes the size, brightness, frequency, position and shape of the images we measure. Therefore, as we probe deeper into space, the knowledge of the geometry of the universe around us will certainly play a crucial role in the data reduction of any survey in the future. With more reliable observational data, one may hope to achieve one of the long term objectives of the current project – being able to *prove* the homogeneity of the observable region of the universe rather than just assuming it in principle.

Acknowledgments

THCL thanks the University of Cape Town and the National Research Foundation for their financial support. CH thanks the National Research Foundation for a research grant.

Appendix A. The near-Parabolic case

One may have noticed from the three evolution equations (4)-(6) that the parabolic evolution is actually the $E \rightarrow 0$ limit of the other two evolutions, which is obtained by writing the functions of η as Taylor expansions for small η and noting that η/\sqrt{E} remains finite. One can see that as we are approaching this borderline case, the evolution equations (4)-(6) are not well-behaved numerically. Also, in reality, it is very difficult, if not impossible, to obtain an exactly parabolic case numerically. Hence, a series expansion is needed in order to have reasonable numerical results for the near-Parabolic case.

Most of the series expansions for the near-Parabolic case can be found in [15]. However, here we will consider the hyperbolic case and give a detailed derivation following the approach in [15], but for obtaining the series expansion for $\tau = t - t_B$ only since this is the only one that is essential to us. Let us first introduce two new variables $x \equiv 2E/M^{2/3}$, and $a \equiv R/M^{1/3}$. The parabolic limit now occurs when $x \rightarrow 0$, while R and τ remain finite. By (4), this requires

$$\eta \rightarrow 0 \text{ and } \frac{\eta}{\sqrt{x}} \rightarrow e \quad (\text{A.1})$$

so that the new evolution parameter e remains finite for finite τ . Taylor series expansion expressions of τ and a for the hyperbolic case using equation (4) are just

$$\tau \approx \frac{e^3}{6} + \frac{xe^5}{120} + \frac{x^2e^7}{5040} + \frac{x^3e^9}{362880} + \dots \quad (\text{A.2})$$

$$a \approx \frac{e^2}{2} + \frac{xe^4}{24} + \frac{x^2e^6}{720} + \frac{x^3e^8}{40320} + \dots \quad (\text{A.3})$$

If we invert the series for a by writing e in series expansion form:

$$e \approx e_0 + e_1x + e_2x^2 + e_3x^3 + \dots, \quad (\text{A.4})$$

then substituting into (A.3), and solving for the coefficients e_i , we get

$$e \approx \sqrt{2a} \left(1 - \frac{1}{12} ax + \frac{3}{160} a^2x^2 - \frac{5}{896} a^3x^3 + \frac{35}{18432} a^4x^4 + \dots \right), \quad (\text{A.5})$$

which we substitute into (A.2), and write it in terms of R , M and E , giving

$$\begin{aligned} \tau \approx \sqrt{\frac{2R^3}{M}} & \left(\frac{1}{3} - \frac{1}{20} \frac{R(2E)}{M} + \frac{3}{224} \frac{R^2(2E)^2}{M^2} - \frac{5}{1152} \frac{R^3(2E)^3}{M^3} \right. \\ & \left. + \frac{35}{22528} \frac{R^4(2E)^4}{M^4} + \dots \right). \end{aligned} \quad (\text{A.6})$$

Equation (A.6) is the τ series expansion expression for the near-parabolic case. One can do the derivation using the elliptic evolution equations similarly.

Appendix B. Coefficients of the series expansions near \hat{R}_{max}

Let us say that \hat{R}_{max} occurs at z_m , $\hat{\mu}n(z_m) = (\hat{\mu}n)_0$, and we define $\Delta z = z - z_m$. So the series expansions for $\hat{\mu}n(z)$, $\hat{R}(z)$, $\phi(z)$, $M(z)$ and $W(z)$ have the form

$$\hat{\mu}n(z) = (\hat{\mu}n)_0 + (\hat{\mu}n)_1\Delta z + (\hat{\mu}n)_2\Delta z^2 + (\hat{\mu}n)_3\Delta z^3 + \dots, \quad (\text{B.1})$$

$$\hat{R}(z) = \hat{R}_{max} + R_2\Delta z^2 + R_3\Delta z^3 + R_4\Delta z^4 + R_5\Delta z^5 + \dots, \quad (\text{B.2})$$

$$\phi(z) = \phi_0 + \phi_1\Delta z + \phi_2\Delta z^2 + \phi_3\Delta z^3 + \dots, \quad (\text{B.3})$$

$$M(z) = M_0 + M_1\Delta z + M_2\Delta z^2 + M_3\Delta z^3 + \dots, \quad (\text{B.4})$$

and

$$W(z) = W_0 + W_1\Delta z + W_2\Delta z^2 + \dots. \quad (\text{B.5})$$

Hence,

$$\frac{d\hat{R}}{dz} = 2R_2\Delta z + 3R_3\Delta z^2 + 4R_4\Delta z^3 + 5R_5\Delta z^4 + \dots, \quad (\text{B.6})$$

and

$$\frac{d^2\hat{R}}{dz^2} = 2R_2 + 6R_3\Delta z + 12R_4\Delta z^2 + 20R_5\Delta z^3 + \dots. \quad (\text{B.7})$$

And the expressions for the coefficients of the series expansion for $M(z)$, $\phi(z)$ and $W(z)$ are given below:

$$M_0 = \frac{\hat{R}_{max}}{2}, \quad (\text{B.8})$$

$$M_1 = M_1, \quad (\text{B.9})$$

$$M_2 = \left(\frac{1}{1+z_m} + \frac{(\hat{\mu}n)_1}{(\hat{\mu}n)_0} \right) \frac{M_1}{2} - \frac{R_2}{2} - \frac{8\pi^2(\hat{\mu}n)_0^2}{\hat{R}_{max}}, \quad (\text{B.10})$$

$$M_3 = \left(-\frac{R_2}{3\hat{R}_{max}} + \frac{(\hat{\mu}n)_2}{3(\hat{\mu}n)_0} + \frac{(\hat{\mu}n)_1}{3(\hat{\mu}n)_0(1+z_m)} \right) M_1 - \frac{1}{4} \left(\frac{R_2}{1+z_m} + \frac{(\hat{\mu}n)_1 R_2}{(\hat{\mu}n)_0} + R_3 \right) - \frac{8\pi^2(\hat{\mu}n)_0(\hat{\mu}n)_1}{\hat{R}_{max}} ; \quad (\text{B.11})$$

$$\phi_0 = \frac{-\hat{R}_{max}R_2}{2\pi(\hat{\mu}n)_0} , \quad (\text{B.12})$$

$$\phi_1 = \left(\frac{(\hat{\mu}n)_1 R_2}{(\hat{\mu}n)_0} - \frac{R_2}{1+z_m} - 3R_3 \right) \frac{\hat{R}_{max}}{4\pi(\hat{\mu}n)_0} , \quad (\text{B.13})$$

$$\phi_2 = \left(\frac{3(\hat{\mu}n)_1 R_3}{2(\hat{\mu}n)_0} - \frac{(\hat{\mu}n)_1^2 R_2}{2(\hat{\mu}n)_0^2} - 4R_4 + \frac{2(\hat{\mu}n)_2 R_2}{3(\hat{\mu}n)_0} - \frac{2R_2^2}{3\hat{R}_{max}} - \frac{3R_3}{2(1+z_m)} + \frac{2(\hat{\mu}n)_1 R_2}{3(\hat{\mu}n)_0(1+z_m)} + \frac{R_2}{2(1+z_m)^2} \right) \frac{\hat{R}_{max}}{4\pi(\hat{\mu}n)_0} , \quad (\text{B.14})$$

$$\phi_3 = \left(-\frac{3(\hat{\mu}n)_1^2 R_3}{4(\hat{\mu}n)_0^2} + \frac{(\hat{\mu}n)_1 R_3}{(\hat{\mu}n)_0(1+z_m)} + \frac{(\hat{\mu}n)_2 R_3}{(\hat{\mu}n)_0} - \frac{3R_2 R_3}{2\hat{R}_{max}} - \frac{R_2}{4(1+z_m)^3} - 5R_5 - \frac{(\hat{\mu}n)_1 R_2}{4(\hat{\mu}n)_0(1+z_m)^2} - \frac{5(\hat{\mu}n)_0^2 R_2}{12(\hat{\mu}n)_0^2(1+z_m)} + \frac{(\hat{\mu}n)_2 R_2}{2(\hat{\mu}n)_0(1+z_m)} - \frac{R_2^2}{2\hat{R}_{max}(1+z_m)} - \frac{2R_4}{1+z_m} + \frac{(\hat{\mu}n)_1^3 R_2}{4(\hat{\mu}n)_0^3} - \frac{2(\hat{\mu}n)_1(\hat{\mu}n)_2 R_2}{3(\hat{\mu}n)_0^2} + \frac{(\hat{\mu}n)_1 R_2^2}{6\hat{R}_{max}(\hat{\mu}n)_0} + \frac{2(\hat{\mu}n)_1 R_4}{(\hat{\mu}n)_0} + \frac{3R_3}{4(1+z_m)^2} + \frac{(\hat{\mu}n)_3 R_2}{2(\hat{\mu}n)_0} \right) \frac{\hat{R}_{max}}{4\pi(\hat{\mu}n)_0} ; \quad (\text{B.15})$$

and

$$W_0 = \frac{M_1}{4\pi(\hat{\mu}n)_0} , \quad (\text{B.16})$$

$$W_1 = \frac{M_1}{4\pi(\hat{\mu}n)_0(1+z_m)} - \frac{R_2}{4\pi(\hat{\mu}n)_0} - \frac{4\pi(\hat{\mu}n)_0}{\hat{R}_{max}} , \quad (\text{B.17})$$

$$W_2 = -\frac{R_2 M_1}{4\pi(\hat{\mu}n)_0 \hat{R}_{max}} - \frac{3R_3}{16\pi(\hat{\mu}n)_0} + \frac{(\hat{\mu}n)_1 R_2}{16\pi(\hat{\mu}n)_0^2} - \frac{3R_2}{16\pi(\hat{\mu}n)_0(1+z_m)} - \frac{2\pi(\hat{\mu}n)_1}{\hat{R}_{max}} . \quad (\text{B.18})$$

Appendix C. The near origin expressions

We do series expansion of equations (A.1) and (A.2) in Appendix A of MHE near the origin, obtaining

$$\hat{R} \approx \frac{1}{H_0} z - \frac{(3+q_0)}{2H_0} z^2 + \frac{4+q_0+q_0^2}{2H_0} z^3 + \dots , \quad (\text{C.1})$$

and

$$4\pi\hat{\mu}n \approx \frac{3q_0}{H_0} z^2 - \frac{6q_0(1+q_0)}{H_0} z^3 + \frac{3q_0(15q_0^2+14q_0+13)}{4H_0} z^4 + \dots . \quad (\text{C.2})$$

We test the accuracy of the generated H_0 and q_0 values using $z = (3/2)\delta z$, and \hat{R} and $4\pi\hat{\mu}n$ values at this same z since this is where we have the first complete set of data according to available observational data and the way we discretise our DEs, and therefore, find the combination with the most consistent accuracy for different q_0 values. We find that in general, using both equations (C.1) and (C.2) with the same number of terms gives us better accuracy. We can then get expressions for H_0 and q_0 near the origin in terms of z , \hat{R} and $4\pi\hat{\mu}n$ only. The results are

$$q_0 = -\frac{\sqrt{(4\pi\hat{\mu}n)^2 + 36\hat{R}^2(2z-1)^2 + 12\hat{R}(4\pi\hat{\mu}n)(10z-7)}}{24z\hat{R}} + \frac{4\pi\hat{\mu}n + 6\hat{R}(1-2z)}{24z\hat{R}}, \quad (\text{C.3})$$

and

$$H_0 = \frac{3q_0z^2(1-2q_0z-2z)}{4\pi\hat{\mu}n}. \quad (\text{C.4})$$

Now we have a way of determining the origin values for H_0 and q_0 from the data. If we need to generate values for r , ϕ , M and W at $z = (1/2)\delta z$ and the origin numerically from the RW expressions given in Appendix A in MHE, then one can perform series expansions of them too, since the values of z are small. They are:

$$M_{RW} \approx \frac{q_0}{H_0}z^3 - \frac{3q_0(1+q_0)}{2H_0}z^4 + \frac{3q_0(3+2q_0+3q_0^2)}{4H_0}z^5 - \frac{q_0(28q_0^3+12q_0^2+15q_0+25)}{8H_0}z^6 + \dots; \quad (\text{C.5})$$

$$\phi_{RW} \approx \frac{1}{H_0} - \frac{2+q_0}{H_0}z + \frac{3q_0^2+4q_0+6}{2H_0}z^2 - \frac{5q_0^3+6q_0^2+6q_0+8}{2H_0}z^3 + \dots; \quad (\text{C.6})$$

$$2E_{RW} \approx (1-2q_0)z^2 - q_0(1-2q_0)z^3 + \frac{1}{4}(1-2q_0)(5q_0^2-2q_0+1)z^4 - \frac{1}{4}(1-2q_0)(7q_0^3-4q_0^2+1)z^5 + \dots; \quad (\text{C.7})$$

$$r_{RW} \approx \frac{1}{H_0}z - \frac{2+q_0}{2H_0}z^2 + \frac{3q_0^2+4q_0+6}{6H_0}z^3 - \frac{5q_0^3+6q_0^2+6q_0+8}{8H_0}z^4 + \dots; \quad (\text{C.8})$$

and these expressions are valid for any q_0 . For $q_0 < 1/2$ and $q_0 > 1/2$ respectively, the τ series expansions for the RW equations take the form:

$$\tau_{RW} \approx \frac{\sqrt{1-2q_0} + q_0 \ln\left(\frac{1-\sqrt{1-2q_0}}{1+\sqrt{1-2q_0}}\right)}{H_0(1-2q_0)^{3/2}} - \frac{1}{H_0}z + \frac{2+q_0}{2H_0}z^2 - \frac{3q_0^2+4q_0+6}{6H_0}z^3 + \frac{5q_0^3+6q_0^2+6q_0+8}{8H_0}z^4 + \dots, \quad (\text{C.9})$$

$$\tau_{RW} \approx \frac{\sin^{-1}\left(\frac{q_0-1}{q_0}\right)q_0 + \frac{\pi}{2}q_0 - \sqrt{2q_0-1}}{H_0(2q_0-1)^{3/2}} - \frac{1}{H_0}z + \frac{2+q_0}{2H_0}z^2 - \frac{3q_0^2+4q_0+6}{6H_0}z^3 + \frac{5q_0^3+6q_0^2+6q_0+8}{8H_0}z^4 + \dots. \quad (\text{C.10})$$

References

- [1] Araújo M E and Stoeger W R 1999 *Phys. Rev. D* **60** 104020 [+ erratum: 2001 *Phys. Rev. D* **64** 049902]
- [2] Araújo M E, Arcuri R C, Bedran M L, de Freitas L R, and Stoeger W R 2001 *Astrophys. J.* **549** 716
- [3] Araújo M E, Roveda S R M M, and Stoeger W R 2001 *Astrophys. J.* **560** 7
- [4] Bishop N and Haines P 1996 *Quaestiones Mathematicae* **19** 259
- [5] Bondi H 1947 *Mon. Not. Roy. Astr. Soc.* **107** 410; reprinted in 1999 *Gen. Rel. Grav.* **11** 1783
- [6] Bondi H, 1960, *Cosmology* (Cambridge University Press, Cambridge)
- [7] Ehlers J, Geren P, and Sachs R K 1968 *J. Math. Phys.* **9** 1344
- [8] Ellis G F R 1971 *General Relativity and Cosmology: Proc. Int. School Phys. "Enrico Fermi" (Varenna) Course XLVII* Ed Sachs R K (Academic press, New York) p 104
- [9] Ellis G F R 1975 *Quart. J. R. Astron. Soc.* **16** 245
- [10] Ellis G F R and Stoeger W R 1987 *Class. Quantum Grav.* **4** 1697
- [11] Ellis G F R, Nel S D, Maartens R, Stoeger W R and Whitman A P 1985 *Phys. Reports* **124** 315
- [12] Hellaby C 1987 *Class. Quantum Grav.* **4** 635
- [13] Hellaby C 2001 *Astron. Astrophys.* **372** 357
- [14] Hellaby C 2006 *Mon. Not. Roy. Astr. Soc.* **370** 239
- [15] Hellaby C and Krasiński A 2006 *Phys. Rev. D* **73** 023518
- [16] Krasiński A and Hellaby C 2004 *Phys. Rev. D* **69** 043502
- [17] Kristian J and Sachs R K 1966 *Astrophys. J.* **143** 379
- [18] Lemaître G 1933 *Ann. Soc. Sci. Bruxelles* **A53** 51; reprinted in 1997 *Gen. Rel. Grav.* **29** 641
- [19] Maartens R and Matravers D R 1994 *Class. Quantum Grav.* **11** 2693
- [20] Mustapha N, Bassett B A C C, Hellaby C and Ellis G F R 1998 *Class. Quantum Grav.* **15** 2363
- [21] Maartens R, Ellis G F R and Stoeger W R 1995 *Quart. J. R. Astron. Soc.* **36** 29
- [22] Mustapha N, Hellaby C and Ellis G F R 1997 *Mon. Not. Roy. Astr. Soc.* **292** 817: "MHE" in the text
- [23] Maartens R, Humphreys N P, Matravers D R and Stoeger W R 1996 *Class. Quantum Grav.* **13** 253 [+ erratum: 1996 *Class. Quantum Grav.* **13** 1689]
- [24] Ribeiro M B and Stoeger W R 2003 *Astrophys. J.* **592** 1
- [25] Sandage A 1961 *Astrophys. J.* **133** 355
- [26] Stoeger W R, Nel S D, Maartens R, and Ellis G F R 1992 *Class. Quantum Grav.* **9** 493
- [27] Stoeger W R, Ellis G F R and Nel S D 1992a *Class. Quantum Grav.* **9** 509
- [28] Stoeger W R, Nel S D and Ellis G F R 1992b *Class. Quantum Grav.* **9** 1711
- [29] Stoeger W R, Nel S D and Ellis G F R, 1992c *Class. Quantum Grav.* **9** 1725
- [30] Stoeger W R, Maartens R and Ellis G F R 1995 *Astrophys. J.* **443** 1
- [31] Tolman R C 1934 *Proc. Nat. Acad. Sci. U.S.A.* **20** 169; reprinted in 1997 *Gen. Rel. Grav.* **29** 935
- [32] Weinberg S 1972 *Gravitation and Cosmology* (Wiley, New York)